On the Tradeoffs Between Coverage Radius, Altitude, and Beamwidth for Practical UAV Deployments

HANEYA NAEEM QURESHI [ID], Graduate Student Member, IEEE
ALI IMRAN, Senior Member, IEEE
School of Electrical and Computer Engineering, The University of Oklahoma, Tulsa, OK USA

Current studies on unmanned aerial vehicle (UAV) based cellular deployment consider UAVs as aerial base stations for air-to-ground communication. However, they analyze UAV coverage radius and altitude interplay while omitting or over-simplifying an important aspect of UAV deployment, i.e., effect of a realistic antenna pattern. This paper addresses the UAV deployment problem while using a realistic three-dimensional directional antenna model. New tradeoffs between UAV design space dimensions are revealed and analyzed in different scenarios. The sensitivity of coverage area to both antenna beamwidth and height is compared. The analysis is extended to multiple UAVs and a new packing scheme is proposed for multiple UAVs coverage that offers several advantages compared to prior approaches.

I. INTRODUCTION

The demand for more diverse, flexible, accessible, and resilient broadband service with higher capacity and coverage is on the rise. Some of these requirements can be accomplished with unmanned aerial vehicles (UAVs) acting as aerial base stations. This is because of the several advantages UAV-based communication offers, such as higher likelihood of line-of-sight (LoS) path and less scatter and signal absorption as compared to terrestrial systems [1], [2]. Moreover, the demand for increase in capacity is leading toward deployment of small cells in terrestrial networks, resulting in the need for higher cell counts, leading to far larger number of ground sites. This makes the goal of attaining seamless coverage over a wide geographical area through terrestrial systems unfeasible due to limited availability of suitable sites and local regulations. This challenge is likely to aggravate with advent of even smaller mmWave cells offering even more sporadic coverage [3].

Similarly, satellite networks have their own limitations, such as high latency, high propagation loss, limited orbit space, and high launching costs [4]. On the contrary, UAVs can be deployed quickly with much more flexibility to move from one point to another, which is a desirable feature for rapid, on-demand, or emergency communications [5]–[7].

UAVs can thus be seen as potential enablers to meet the several challenges of next generation wireless systems by either functioning as complementary architecture with already existing cellular networks to compensate for cell overload during peak times and emergency situations [8], [9] or by serving as stand-alone architecture to provide new infrastructure, especially in remote areas [10]–[12]. In this domain, a new hybrid network architecture for cellular systems by leveraging the use of UAVs for data offloading is proposed in [9] and [13]. Another significant application of UAVs is in the emerging Internet of Things (IoT) technology [14] and wireless sensor networks [15], where low altitude UAVs can provide a means to collect the IoT data from devices with limited transmit power and transmit it to their intended receivers.

However, in order to fully reap the benefits of UAV-based communication, optimal design of UAVs deployment parameters is of fundamental importance. In this paper, we address the UAV deployment problem by analyzing the tradeoffs between key system design parameters, such as height, antenna beamwidth, and number of UAVs. By leveraging a more realistic model compared to prior studies on the topic, our analysis reveals several new insights and tradeoffs between the design parameters that remain unexplored in existing studies.

A. Related Work

Several studies have recently addressed UAV deployment for different service requirements, mostly using altitude, transmission power, and number of UAVs as the only three deployment parameters. For example, Al-Hourani *et al.* in [16] investigate the maximum coverage and optimal altitude assuming one UAV with no interference. The

optimal altitude is estimated as a function of maximum allowed path loss and statistical parameters of urban environment. However, this paper is limited to a single UAV while using mean value of shadowing (rather than its random behavior) and altitude as the only optimization parameter to control coverage. In [17], Al-Hourani et al. determine optimal height for maximum coverage for a single UAV based on coverage probability and the information rate of users on the ground at a particular UAV altitude.

Mozaffari et al. in [18] extend the work in [16] and [17] to two UAVs, with and without interference. Based on the path loss models in [16] and [19], optimal altitude is reported in [18] for both maximum coverage and minimum required transmit power. Continuing to analyze altitude versus coverage radius relationship, in [20], the same team of authors addresses the deployment problem with coexistence between UAV and under laid device-to-device communication networks.

Apart from coverage area, other performance indicators are also affected by changes in UAV height, such as carrier-to-interference ratio and handovers. Focusing on mmWave band, Thornton et al. in [21] investigate coverage versus carrier-to-interference ratio patterns using an antenna pattern approximated by a cosine function rose to a power. Building upon the work in [21], the effect of lateral displacement of a UAV on interference and handovers is studied in [22]. Goddemeier et al. in [23] measure received signal strength (RSS) indicator for three UAV-based cellular networks using following models: Okumura–Hata, COST Hata, and COST Walfish–Ikegami. It is reported that signal strengths decrease faster with increase in altitude. However, this paper considers UAVs up to an altitude of 500 m because of their path loss models constraints. Focusing on just the altitude as a deployment parameter, study in [24] investigates the altitude estimation of UAVs from a more practical perspective using measurements of the polarization of magnetic field of low-frequency radio signals. Mahmood et al. in [25] estimate the relative attitude between two communicating UAV nodes where the nodes are equipped with multiple-input multiple-output (MIMO) antenna arrays with diverse polarization.

Other works that study UAV deployment from the perspective of optimal altitude and coverage radius include [26]–[28]. The proposed algorithm in [26] finds the optimal altitude of UAV based on the desired radius of coverage in real time. Another deployment model is considered in [27], in which the coverage area is calculated numerically by considering the altitude of UAV and the location of both UAV and users in the horizontal dimension. Results show that the size of the coverage area is affected by the environment. Ideas introduced in [27] are further elaborated in [28] leading to the conclusion that larger buildings require a higher UAV altitude. Additionally, network coverage through a cognitive relay node network model with a goal to enhance the performance of standard relay nodes is addressed in [28].

Optimal trajectory designs are studied in [29] by considering a constant UAV height. Joint optimization of UAV's trajectory, as well as the bandwidth allocation and user partitioning between the UAV and ground base stations are analyzed in [9] and [13]. The authors in these studies aim to maximize the minimum throughput of all mobile terminals in the cell and consider orthogonal spectrum sharing between the UAV and ground base stations. The framework is extended to the spectrum reuse case and results show that the proposed hybrid network with optimized spectrum sharing and cyclical multiple access design significantly improves the spatial throughput over terrestrial networks, whereas the spectrum reuse scheme can provide further throughput gains compared to orthogonal spectrum sharing. Other UAV trajectory designs are considered in [30]–[32]. Zeng et al. in [30] aim to design the UAV trajectory to minimize its mission completion time while ensuring that each ground station successfully recovers the file with a desired high probability. Optimization of multiuser communication scheduling and association jointly with the UAV's trajectory and power control is addressed in [31]. Two other practical types of UAV trajectories, namely circular flight and straight flight are considered in [32] in order to characterize the energy tradeoff in ground-to-UAV communication. Another interesting tradeoff between throughput and delay from the perspective of trajectory optimization is studied in [33]. In this paper, a new cyclical multiple access scheme is proposed to schedule the communications between the UAV and ground terminals in a cyclical time-division manner based on the flying UAV's position. Under this scheme, Lyu et al. in [33] reveal a fundamental tradeoff between throughput and access delay.

UAV-based relay network optimizations are studied in [34]–[36]. Compared with conventional static relaying, Zeng et al. in [36] consider mobile relaying, which offers a new degree of freedom for performance enhancement via careful relay trajectory design. The authors in this work show that by optimizing the trajectory of the relay and power allocations adaptive to its induced channel variation, mobile relaying is able to achieve significant throughput gains over the conventional static relaying. Holis et al. in [37] consider the impact of antenna power rolloff in 3G networks for fixed platform height and propose a gain adjustment strategy for circular beam antennas.

However, none of the aforementioned studies [16]–[37] consider the impact of antenna gain pattern on the coverage versus height tradeoff. One recent study that takes into account effect of directional antenna considers joint altitude and beamwidth optimization for UAV-enabled multiuser communications [38]. In this study, users are partitioned into disjoint clusters and the UAV sequentially serves all clusters by hovering above the cluster centers one by one. In [38], He et al. consider three communication models: downlink multicasting, downlink broadcasting, and uplink multiple access. One distinguishing feature of [38] is the conclusion that optimal beamwidth and height critically depend on the communication model considered. However, this study uses a stepwise antenna gain model for analytical tractability and LoS propagation conditions. Another recent study [39] that does consider the effect of antenna

also uses a stepwise antenna gain model with only two possible values of antenna gain. Analysis incorporating realistic antenna model has become more important since several studies are already considering implementations of directional antenna in UAV-based cellular systems [40], such as smart WiFi directional antennas with servo motors [41]. While the UAV deployment problem has been investigated in a large number of recent studies as discussed earlier, to the best of authors' knowledge, this is the first paper to study the optimization of UAV deployment design parameters while using a realistic three-dimensional (3-D) directional antenna model in the system. The analysis presented in this paper shows that the use of a realistic antenna pattern makes a trend shifting difference in the height versus coverage tradeoff and adds a new dimension of beamwidth to the UAV deployment design space that remains unexamined in earlier studies.

B. Contributions and Organization

The contributions and organization of this paper can be summarized as follows.

1) We develop a mathematical framework for UAV deployment design while incorporating a realistic model for a practical directional antenna. Current studies on UAV deployment either ignore the effect of 3-D directional antenna [16]–[35] or consider an over-simplified model for antenna gain [38], [39]. Therefore, UAV deployment analysis presented in such studies, yields results on optimal height, coverage radius and number of UAVs that may not hold for real UAV deployments with practical directional antenna. We address this problem by using 3GPP defined 3-D parabolic antenna pattern whose gain is realistically dependent on not only beamwidth but also 3-D elevation angle (see Sections II and III-A).

2) We derive analytical expressions for coverage characterized by RSS as a function of height, beamwidth, and coverage radius (see Sections II and III-B).

3) We present a mathematical framework to quantitatively analyze tradeoffs among the following parameters: cell radius versus beamwidth for varying heights, cell radius versus height for different beamwidths, and beamwidth versus height for different coverage radii. To the best of authors' knowledge, this paper is first to investigate this interesting interplay among the five key factors that define UAV-based coverage design space: antenna beamwidth and angular distance dependent gain, elevation angle dependent probability of LoS, shadowing, free space path loss, and height (see Section IV-A).

4) We investigate the impact of key UAV design parameters on RSS and validate our derived expressions for probability density function (PDF) of RSS through simulations (see Section IV-B, IV-C, and IV-D).

5) The proposed framework is extended to a range of frequencies and environments (see Section IV-C).

6) Prior works on UAV deployment design [16], [17], [39] use UAV altitude as the only optimization parameter to control coverage. Contrary to the findings from these prior studies, based on our joint analysis of effect of beamwidth and altitude on coverage, we show the following.

a) There exists an optimal beamwidth for given height for maximum coverage radius and vice versa. We also derive an expression for determining optimal beamwidth/height for desired coverage radius.

b) Antenna beamwidth is a more practical design parameter to control coverage instead of UAV altitude. This is concluded by performing comparative analysis of the two by quantifying the sensitivity of coverage to both height and beamwidth (see Section IV-E).

c) Contrary to what has been assumed implicitly or explicitly in prior studies, UAV altitude cannot be optimized independent of antenna beamwidth. In fact, both parameters need to be optimized in tandem with each other to plan true coverage.

7) Coverage probability patterns with varying tilt angles and asymmetrical beamwidths are presented in Section IV-F, which highlight the capability of our derived equations and the underlying system model to extend the analysis to a wide range of scenarios, such as nonzero tilt angle and asymmetrical beamwidths.

8) We also extend the analysis to multiple UAVs. Some recent studies have leveraged circle packing theory to determine the number of UAVs needed to cover a given area [39]. However, this approach has two caveats: First, it leaves significant coverage holes when two or more UAVs are used to cover an area. Second, the number of UAVs increase dramatically with increase in required coverage probability. To circumvent the problems posed by circle packing theory, we propose use of hexagonal packing and compare our results with that obtained by circle packing. This comparison identifies several further advantages of proposed approach (see Section IV-G).

9) Continuing our analysis on multiple UAVs, we determine the optimal beamwidth for different number of UAVs that yields maximum total coverage for a target geographical area (see Section IV-G). Results show that proposed multi-UAV deployment framework can meet same coverage requirements with less infrastructure (number of UAVs) compared to existing model [39].

The key findings of this paper are concluded in Section V.

II. SYSTEM MODEL

We consider a system model illustrated in Fig. 1. The UAV resides at a height h and projects a cell with coverage radius r when $\phi_{\text{tilt}} = 0°$. We define UAV coverage area as a set of points in circle of radius r, where a mobile station (MS) experiences an RSS, S_r above a threshold γ. Here, r is measured from the projection of UAV on ground. In Fig. 1, ϕ_{tilt} is the tilt angle in degrees of the antenna mounted on UAV and ϕ_{MS} is the vertical angle in degrees from the reference axis (for tilt) to the MS. θ_a is the angle of orientation of the antenna with respect to

TABLE I
Key Symbol Definitions

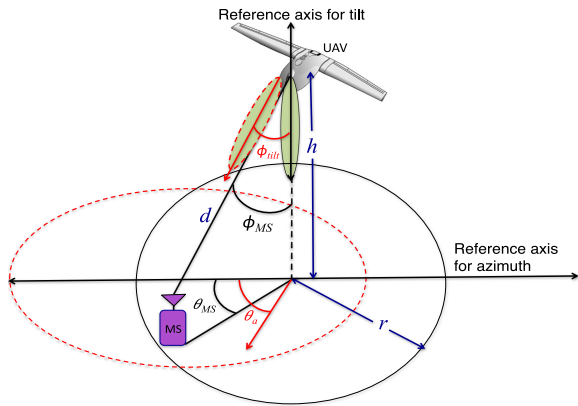| Sym.	Units	Definition	Sym.	Units	Definition
h	m	height of UAV	P_l	-	probability of LoS scenario
r	m	coverage radius	P_n	-	probability of NLoS scenario
d	m	UAV to MS distance	c	m/s	speed of light
X_l	dB	RV for location variability in LoS scenario	X_n	dB	RV for location variability in NLoS scenario
σ_l	dB	standard deviation of X_l	σ_n	dB	standard deviation of X_n
ϕ_{tilt}	°	tilt angle of antenna	PL_{max}	dB	maximum path loss
ϕ_{MS}	°	vertical angle from tilt reference axis to MS	θ_a	°	angle of antenna w.r.t horizontal reference axis
f	GHz	frequency	X_s	dB	RV shadowing
θ_{MS}	°	angular distance of MS	σ_{s_n}	dB	standard deviation of S_n
B_ϕ	°	3dB beamwidth with respect to ϕ direction	B_θ	°	3dB beamwidth with respect to θ direction
μ'_n	dB	mean of X'_n	μ_{sh}	dB	mean of X_s
σ'_n	dB	standard deviation of X'_n	σ_{sh}	dB	standard deviation of X_s
λ_ϕ	-	weighting factor for beam pattern in ϕ direction	λ_θ	-	weighting factor for beam pattern in θ direction
R_t	km	radius of desired geographical area	ϵ	-	minimum coverage probability
G	dB	antenna gain	γ	dBm	received signal threshold
R_l	dBm	received signal strength in LoS scenario	R_n	dBm	received signal strength in NLoS scenario
S_n	dBm	product of received signal strength in NLoS scenario and probability of NLoS scenario at any r: $S_n = P_n R_n$	S_l	dBm	product of received signal strength in LoS scenario and probability of LoS scenario at any r: $S_l = P_l R_l$
B	°	beamwidth for circular beam pattern	G_{max}	dB	maximum antenna gain at bore sight
S_r	dBm	received signal strength at any r: $S_r = S_l + S_n$	S	dBm	received signal strength inside a geographical region
P_{cov}	-	coverage probability	μ_s	-	mean of S_r
$A_{\max}$	dB	maximum antenna attenuation at sides and back of bore sight	σ_{s_l} σ_s	dB dB	standard deviation of S_l standard deviation of S_r
T	dBm	transmit signal	$f_S(s)$	-	PDF of S
N	-	number of UAVs	$f_{S_r}(s_r)$	-	PDF of S_r

Fig. 1.   System model.

horizontal reference axis, i.e., positive x-axis and θ_{MS} is the angular distance of MS from the horizontal reference axis.

$$G(\phi_{MS}, \phi_{tilt}, \theta_{MS}, \theta_a, B_\phi, B_\theta)$$

$$= \lambda_\phi \left(G_{\max} - \min\left(12\left(\frac{\phi_{MS} - \phi_{tilt}}{B_\phi}\right)^2, A_{\max}\right)\right)$$

$$+ \lambda_\theta \left(G_{\max} - \min\left(12\left(\frac{\theta_{MS} - \theta_a}{B_\theta}\right)^2, A_{\max}\right)\right) \quad (1)$$

Utilizing the geometry in Fig. 1, the perceived antenna gain from the UAV using a 3-D antenna model recommended by 3GPP [42], at the location of MS can be represented as in (1). Here, B_θ and B_ϕ represent the horizontal half power beamwidth (with respect to the θ-direction) and the vertical half power beamwidth (with respect to ϕ-direction) of the UAV antenna in degrees, respectively, whereas λ_θ and λ_ϕ represent the weighting factors for the beam pattern in both directions, respectively. $G_{\max}$ and $A_{\max}$ denote the maximum antenna gain in decibel at the boresight of the antenna and maximum attenuation at the sides and back of boresight, respectively. $G_{\max}$ can be approximated as $10\log\left(\frac{29000}{B_\phi B_\theta}\right)$ [43].

The air-to-ground channel can be characterized in terms of probabilities of LoS and non-LoS (NLoS) scenarios between the UAV and MS. Prior studies have used channel models proposed in [19], [44], and [45]. The channel models proposed in [19] and [44] are suited to only dense urban and typical European cities, respectively. Moreover, channel models presented in [19] and [44] lack measurement based validation. On the other hand, the channel model in [45] not only provides a simulation based data for a diverse range of elevation angles, environments, and frequencies, but also has been validated through extensive empirical measurements. Hence, we use the UAV channel model pro-

TABLE III
Frequency-Dependent Parameters for Shadowing

f (GHz)		p_v	q_v	t_v
2.0	$v = \mu$	-94.20	-3.44	0.0318
	$v = \sigma$	-89.55	-8.87	0.0927
3.5	$v = \mu$	-92.90	-3.14	0.0302
	$v = \sigma$	-89.06	-8.63	0.0921
5.5	$v = \mu$	-92.80	-2.90	0.0285
	$v = \sigma$	-89.54	-8.47	0.9000

posed in [45] to estimate the probability of LoS scenario as follows:

$$P_l(\phi_{\text{MS}}) = 0.01j - \frac{0.01(j-k)}{1 + \left(\frac{90-\phi_{\text{MS}}-l}{m}\right)^n} \tag{2}$$

where $(j, \ldots, n)$ are the set of empirical parameters for different types of environments and are given in Table II. The angle $90 - \phi_{\text{MS}} = \tan^{-1}(\frac{h}{r})$ is the angle of elevation of the MS to the UAV. The probability of NLoS scenario is then $1 - P_l(\phi_{\text{MS}})$.

In addition to free space path loss, UAV-MS signal faces an elevation angle dependent shadowing. The mean and standard deviation for this shadowing can be modeled as [45]

$$\mu_{\text{sh}} = \frac{p_\mu + (90 - \phi_{\text{MS}})}{q_\mu + t_\mu(90 - \phi_{\text{MS}})} \tag{3}$$

$$\sigma_{\text{sh}} = \frac{p_\sigma + (90 - \phi_{\text{MS}})}{q_\sigma + t_\sigma(90 - \phi_{\text{MS}})} \tag{4}$$

where p_μ, q_μ, t_μ, p_σ, q_σ, and t_σ are parameters obtained from empirical measurements given in Table III. In Table III, the subscript $v = \{\mu, \sigma\}$ is used to indicate that the parameters are for mean and standard deviation, respectively. The RSS in LoS and NLoS scenarios, as a function of path loss and antenna gain can now be

represented as

$$R_l(\phi_{\text{MS}}, \phi_{\text{tilt}}, \theta_{\text{MS}}, \theta_a, B_\phi, B_\theta, d) = T - 20\log\left(\frac{4\pi f d}{c}\right)$$
$$+ G(\phi_{\text{MS}}, \phi_{\text{tilt}}, \theta_{\text{MS}}, \theta_a, B_\phi, B_\theta) - X_l \tag{5}$$

$$R_n(\phi_{\text{MS}}, \phi_{\text{tilt}}, \theta_{\text{MS}}, \theta_a, B_\phi, B_\theta, d) = T - 20\log\left(\frac{4\pi f d}{c}\right)$$
$$+ G(\phi_{\text{MS}}, \phi_{\text{tilt}}, \theta_{\text{MS}}, \theta_a, B_\phi, B_\theta) - X_n - X_s \tag{6}$$

where T is transmitted power, c is the speed of light, f denotes the frequency, d is the distance between UAV and MS, and X_s is shadow fading Gaussian $\mathcal{N}(\mu_{\text{sh}}, \sigma_{\text{sh}})$ random variable (RV) with mean μ_{sh} and standard deviation σ_{sh}. X_s is part of the received signal strength in NLoS scenario only because shadowing is a phenomenon associated exclusively with NLoS scenario due to the presence of obstacles in NLoS scenario, which affect wave propagation [45]. For realistic system level modeling of mobile systems, random components in decibel X_l and X_n are added as environment-dependent variables in LoS and NLoS scenarios [45]. Note that in LoS scenario, despite having a direct path between the UAV and MS, reflections from scatters in the surrounding of the MS can result in different signal strength at different MS locations even when the MS locations are at same distance from the UAV and have LoS. This location-dependent randomness in the received signal in LoS scenario is captured in the form of RV X_l with log-normal distribution of mean zero. X_l and X_n are therefore $\mathcal{N}(0, \sigma_l)$ and $\mathcal{N}(0, \sigma_n)$ RVs, where σ_l and σ_n denote the standard deviations, in decibel, of X_l and X_n, respectively. Key symbol definitions along with their units are defined in Table I.

III. UAV COVERAGE MODEL DEVELOPMENT

A. Coverage Probability

As described in Section II, we define UAV coverage area as a set of points in circle of radius r, where an MS experiences an RSS S_r above a threshold γ. Then, the RSS at the boundary exceeds a certain threshold $\gamma = T - \text{PL}_{\text{max}}$ with a probability $P_{\text{cov}} \geq \epsilon$, where PL_{max} is the maximum allowable path loss. We define this coverage probability P_{cov} as

$$P_{\text{cov}} = \text{P}[S_r \geq \gamma]$$
$$= P_l(\phi_{\text{MS}})\text{P}[R_l(\phi_{\text{MS}}, \phi_{\text{tilt}}, \theta_{\text{MS}}, \theta_a, B_\phi, B_\theta, d) \geq \gamma]$$
$$+ P_n(\phi_{\text{MS}})\text{P}[R_n(\phi_{\text{MS}}, \phi_{\text{tilt}}, \theta_{\text{MS}}, \theta_a, B_\phi, B_\theta, d) \geq \gamma] \tag{7}$$

$$\text{P}\left[R_n\left(\phi_{\text{MS}}, \phi_{\text{tilt}}, \theta_{\text{MS}}, \theta_a, B_\phi, B_\theta, d\right) \geq \gamma\right] = \text{P}\left[T + G(\phi_{\text{MS}}, \phi_{\text{tilt}}, \theta_{\text{MS}}, \theta_a, B_\phi, B_\theta) - 20\log\left(\frac{4\pi f d}{c}\right) - X_n - X_s \geq \gamma\right] \tag{8}$$

$$= \int_\gamma^\infty \frac{1}{\sqrt{2\pi}\sigma_n'} \exp\left[-\frac{1}{2}\left(\frac{X_n' - \left(T + G(\phi_{\text{MS}}, \phi_{\text{tilt}}, \theta_{\text{MS}}, \theta_a, B_\phi, B_\theta) - 20\log\left(\frac{4\pi f d}{c}\right) - \mu_n'\right)}{\sigma_n'}\right)^2\right] dX_n' \tag{9}$$

$$= Q\left(\frac{20\log\left(\frac{4\pi f d}{c}\right) + \mu_{\text{sh}} - G(\phi_{\text{MS}}, \phi_{\text{tilt}}, \theta_{\text{MS}}, \theta_a, B_\phi, B_\theta) - \text{PL}_{\text{max}}}{\sqrt{\sigma_{\text{sh}}^2 + \sigma_n^2}}\right) \tag{10}$$

First, we calculate $P[R_n(\phi_{MS}, \phi_{tilt}, \theta_{MS}, \theta_a, B_\phi, B_\theta, d) \geq \gamma]$ using (6) as in (8)–(10) shown at the bottom of the previous page, where (10) is a result of complementary cumulative distribution function (CDF) of a Gaussian RV and substituting $\gamma = T - PL_{max}$ in (9) and $G(\phi_{MS}, \phi_{tilt}, \theta_{MS}, \theta_a, B_\phi, B_\theta)$ is defined in (1). Without loss of generality, we assume X_n and X_s to be independent RVs, and thus, $X'_n = X_n + X_s$ with mean $\mu'_n = \mu_{sh}$ and standard deviation $\sigma'_n = \sqrt{\sigma_{sh}^2 + \sigma_n^2}$.

Similarly, we derive $P[R_l(\phi_{MS}, \phi_{tilt}, \theta_{MS}, \theta_a, B_\phi, B_\theta, d) \geq \gamma]$, which yields the following expression:

$$P\left[R_l\left(\phi_{MS}, \phi_{tilt}, \theta_{MS}, \theta_a, B_\phi, B_\theta, d\right) \geq \gamma\right]$$
$$= Q\left(\frac{20\log\left(\frac{4\pi fd}{c}\right) - G(\phi_{MS}, \phi_{tilt}, \theta_{MS}, \theta_a, B_\phi, B_\theta) - PL_{max}}{\sigma_l}\right) \tag{11}$$

where $Q(z) = \frac{1}{\sqrt{2\pi}} \int_z^\infty \exp(\frac{-u^2}{2})du$.

Moreover, from cell geometry in Fig. 1 (under the assumption: height of MS $<< h$ and the UAV is located at coordinates $(x, y, z) = (0, 0, h)$, where x and y are the Cartesian coordinates of MS on ground), ϕ_{MS} and d can be expressed as:

$$\phi_{MS} = \tan^{-1}\left(\frac{\sqrt{x^2 + y^2}}{h}\right), d = \sqrt{h^2 + x^2 + y^2}. \tag{12}$$

The probability of coverage at a particular location of user on ground can now be found by substituting (2), (10), and (11) in (7), which yields the expression given in (13) shown at the bottom of this page.

However, since UAVs are mobile and can rapidly move from one location to another to provide on-demand coverage where needed, for most practical scenarios, a circular coverage pattern is considered, rather than tampering with antenna tilt. A special case of (13), in which the horizontal and vertical antenna beamwidths are symmetric, i.e., $B_\phi = B_\theta = B$ and $\phi_{tilt} = 0°$ results in circular coverage

footprint of the received signal strength on ground. Note that with $\phi_{tilt} = 0°$, the azimuth plane becomes perpendicular to the boresight and the second part of (1) is no longer applicable. In this scenario

$$r = \sqrt{x^2 + y^2}, \phi_{MS} = \tan^{-1}\left(\frac{r}{h}\right), d = \sqrt{h^2 + r^2}. \tag{14}$$

Furthermore, G_{max} can be approximated as $10\log\left(\frac{29000}{B^2}\right)$ [43] and A_{max} can be ignored without impacting the required accuracy of this antenna model that mainly concerns gain on and around the boresight. Applying these simplifications to (1), substituting (1) and (14) in (10) and (11) and then making use of (7) yields the expression for P_{cov} as a function of antenna beamwidth, UAV height, and coverage radius in (15) shown at the bottom of this page.

B. Received Signal Strength

One way to investigate the RSS on a particular location on ground for a given height and antenna beamwidth for circular coverage pattern is by evaluating the expected value of S_r over the RVs X_s, X_l, and X_n as follows:

$$\mathbf{E}[S_r] \overset{(k)}{=} P_l \mathbf{E}[S_r|LoS] + P_n \mathbf{E}[S_r|NLoS]$$
$$= P_l \mathbf{E}[R_l - R_n] + \mathbf{E}[R_n]$$
$$= \left(0.01j - 1 - \frac{0.01(j-k)}{1 + \left(\frac{\tan^{-1}(\frac{h}{r}) - l}{m}\right)^n}\right)\mu_{sh} - 20\log\left(\frac{4\pi fd}{c}\right)$$
$$+ T - 12\left(\frac{\tan^{-1}\left(\frac{r}{h}\right) - \phi_{tilt}}{B}\right)^2 + 10\log\left(\frac{29000}{B^2}\right) \tag{16}$$

where (k) is a result of the law of total expectation and P_l, R_l, and R_n are functions of r, h, and B and defined in (2), (5), and (6), respectively. Equation (16) is therefore obtained by substituting R_l and R_n from (5) and (6) and then making use of the relationship between $P_l(\phi_{MS})$ and $P_n(\phi_{MS})$, i.e., $P_n(\phi_{MS}) = 1 - P_l(\phi_{MS})$.

$$P_{cov}(\phi_{MS}, \phi_{tilt}, \theta_{MS}, \theta_a, d, B_\theta, B_\phi) = \left(0.01j - \frac{0.01(j-k)}{1 + \left(\frac{90-\phi_{MS}-l}{m}\right)^n}\right)Q\left(\frac{20\log\left(\frac{4\pi fd}{c}\right) - G(\phi_{MS}, \phi_{tilt}, \theta_{MS}, \theta_a, B_\phi, B_\theta) - PL_{max}}{\sigma_l}\right)$$
$$+ \left(1 - 0.01j + \frac{0.01(j-k)}{1 + \left(\frac{90-\phi_{MS}-l}{m}\right)^n}\right)Q\left(\frac{20\log\left(\frac{4\pi fd}{c}\right) + \mu_{sh} - G(\phi_{MS}, \phi_{tilt}, \theta_{MS}, \theta_a, B_\phi, B_\theta) - PL_{max}}{\sqrt{\sigma_{sh}^2 + \sigma_n^2}}\right) \tag{13}$$

$$P_{cov}^c(r, h, B) = \left(0.01j - \frac{0.01(j-k)}{1 + \left(\frac{\tan^{-1}(\frac{h}{r}) - l}{m}\right)^n}\right)Q\left(\frac{20\log\left(\frac{4\pi f\sqrt{h^2+r^2}}{c}\right) - 10\log\left(\frac{29000}{B^2}\right) + 12\left(\frac{\tan^{-1}\left(\frac{r}{h}\right) - \phi_{tilt}}{B}\right)^2 - PL_{max}}{\sigma_l}\right)$$
$$+ \left(1 - 0.01j + \frac{0.01(j-k)}{1 + \left(\frac{\tan^{-1}(\frac{h}{r}) - l}{m}\right)^n}\right)Q\left(\frac{20\log\left(\frac{4\pi f\sqrt{h^2+r^2}}{c}\right) + \mu_{sh} - 10\log\left(\frac{29000}{B^2}\right) + 12\left(\frac{\tan^{-1}\left(\frac{r}{h}\right) - \phi_{tilt}}{B}\right)^2 - PL_{max}}{\sqrt{\sigma_{sh}^2 + \sigma_n^2}}\right) \tag{15}$$

However, R_l is an RV due to the random component X_l and R_n is an RV due to the random components X_n and X_s. Therefore, RSS can also be modeled as an RV. In order to derive an analytical expression for the PDF of RSS at any arbitrary cell location, we express it as

$$S_r(h, r, B) = S_l(h, r, B) + S_n(h, r, B) \qquad (17)$$

where S_l and S_n are independent RVs, given by $S_l(h, r, B) = P_l(\phi_{\text{MS}})R_l(h, r, B)$ and $S_n(h, r, B) = P_n(\phi_{\text{MS}})R_n(h, r, B)$, respectively. Then, in order to derive an analytical expression for PDF of S_r, we resort to transformations of RVs and convolution of the PDFs of S_l and S_n, resulting in the expression in (18) shown at the bottom of this page. Complete derivation of (18) is provided in Appendix.

The normalized PDF of received signal strength inside a geographical region (denoted by S) by assuming that the UAV resides at coordinates $(x, y, z) = (0, 0, h)$, where h is height of UAV, can then be found as follows:

$$f_S(s) = \frac{1}{A} \iint_A f_{S_r}(s, x, y)dxdy \qquad (19)$$

in some geographical region A that lies in the xy-plane. The integral in (19) can be solved through numerical methods.

IV. NUMERICAL RESULTS AND ANALYSIS

A. TradeOffs Between Coverage Radius, Beamwidth, and Height

1) Coverage Radius Versus Beamwidth: As the height of UAV increases for a particular MS location, ϕ_{MS} in (14) decreases (angle of elevation increases), leading to an increase in probability of LoS link in (2), decrease in shadowing in (4), and increase in free space path loss (as d increases). While the effect of these factors on coverage has been studied in earlier studies [16]–[37], the impact of the fourth factor, antenna gain in conjunction with these three factors remained unexamined. Fig. 2 shows that the impact of this fourth factor is so profound that at a given cell radius, it results in a height (h'), after which the antenna gain trend with increasing beamwidth reverses. Fig. 2 is plotted utilizing (1) for $\phi_{\text{tilt}} = 0°$ at $r = 5000$ m under the assumptions stated in Section III. The larger antenna gain at a given r is observed with increased height because, for the same MS location, ϕ_{MS} in (14) decreases. For any two beamwidths, B_1 and B_2, h' is the point of intersection of gain versus
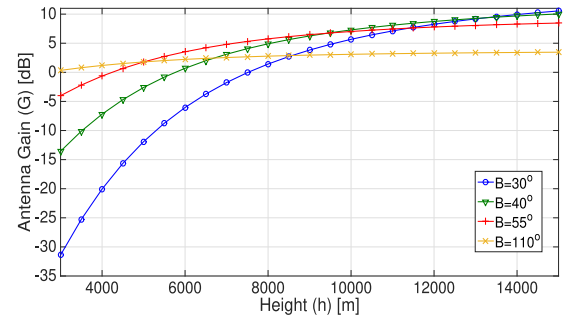

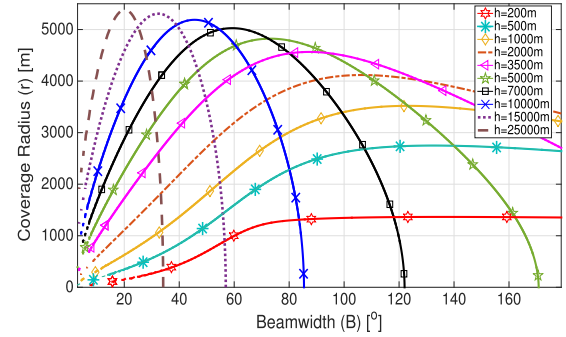Fig. 2. Antenna gain at $r = 5000$ m with varying heights for different beamwidths.

Fig. 3. Coverage radius against beamwidth for different heights.

height graphs illustrated in Fig. 2 for $r = 5000$ m. h' can be calculated as follows:

$$10\log\left(\frac{29000}{B_1^2}\right) - 12\left(\frac{\tan^{-1}\left(\frac{r}{h'}\right)}{B_1}\right)^2$$
$$= 10\log\left(\frac{29000}{B_2^2}\right) - 12\left(\frac{\tan^{-1}\left(\frac{r}{h'}\right)}{B_2}\right)^2$$
$$h' = r\left(\tan\sqrt{\frac{5}{3}\log\left(\frac{B_2}{B_1}\right)\left(\frac{B_1^2 B_2^2}{B_2^2 - B_1^2}\right)}\right)^{-1}. \qquad (20)$$

The coverage radius versus beamwidth trend for different heights in Fig. 3 can now be analyzed in light of the aforementioned factors. This figure is plotted by utilizing (15) for $\text{PL}_{\max} = 115$ dB, $\phi_{\text{tilt}} = 0°$, $\epsilon = 0.8$, and $f = 2$ GHz in a suburban environment. The trend shift in Fig. 3 is attributed to the following: as height increases up to 1000 m, the increase in antenna gain and decrease in shadowing

$$f_{S_r}(s_r) = \frac{\exp\left[\frac{-\left[s_r - \left(1 - 0.01j + \frac{0.01(j-k)}{1+\left(\frac{\tan^{-1}(h/r)-l}{m}\right)^n}\right)\left(\frac{p_\mu + \tan^{-1}(h/r)}{q_\mu + t_\mu \tan^{-1}(h/r)}\right) - T + 20\log\left(\frac{4\pi f\left(\sqrt{h^2+r^2}\right)}{c}\right) - 10\log\left(\frac{29000}{B^2}\right) + 12\left(\frac{\tan^{-1}(r/h)}{B}\right)^2\right]^2}{2\sigma_l^2\left(\frac{0.01(j-k)}{1+\left(\frac{\tan^{-1}(h/r)-l}{m}\right)^n}\right)^2 + \left(1 - \frac{0.01(j-k)}{1+\left(\frac{\tan^{-1}(h/r)-l}{m}\right)^n}\right)^2\left(\sigma_n^2 + \left(\frac{p_\sigma + \tan^{-1}(h/r)}{q_\sigma + t_\sigma \tan^{-1}(h/r)}\right)^2\right)}\right]}{\sqrt{2\pi\sigma_l^2\left(\frac{0.01(j-k)}{1+\left(\frac{\tan^{-1}\left(\frac{h}{r}\right)-l}{m}\right)^n}\right)^2 + \left(1 - \frac{0.01(j-k)}{1+\left(\frac{\tan^{-1}\left(\frac{h}{r}\right)-l}{m}\right)^n}\right)^2\left(\sigma_n^2 + \left(\frac{p_\sigma + \tan^{-1}\left(\frac{h}{r}\right)}{q_\sigma + t_\sigma \tan^{-1}\left(\frac{h}{r}\right)}\right)^2\right)}} \qquad (18)$$

Fig. 4. Coverage radius against height for different beamwidths.
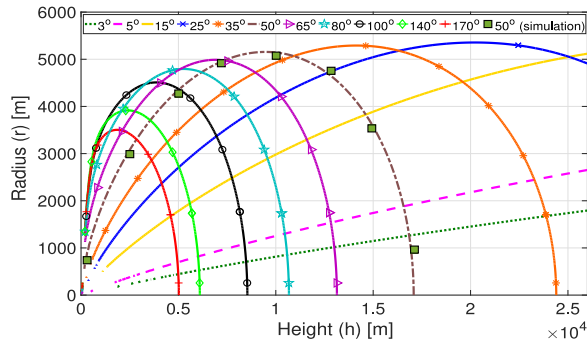

Fig. 5. Beamwidth against height for different radii.

offset the increased free space path loss. As height increases beyond 1000 m, the increase in antenna gain and decrease in shadowing are overshadowed by the increase in free space loss. As a result, the coverage radius increases with beamwidth, approaches to a maximum value and then starts to decrease. Our analysis quantifies this maximum value of coverage radius in relation to antenna gain, for instance, maximum coverage radius of 5000 m at a beamwidth of $55°$ for $h = 7000$ m in Fig. 3 can be attributed to the occurrence of largest antenna gain at a beamwidth of $55°$ at a height of 7000 m in Fig. 2.

Our UAV coverage model for the first time shows the existence of optimal beamwidth for given height for maximum coverage radius and vice versa, a trend that remains hidden in UAV coverage models presented in prior studies [16]–[39].

2) *Coverage Radius Versus Height:* Fig. 4 depicts the relation of coverage radius with height for different beamwidths. Initially, as the height of the UAV increases for small beamwidths, coverage radius also increases continuously. However, as beamwidth increases further, coverage radius versus height curves attain a parabolic shape. This is in contrast to previous studies that suggest monotonic increase of UAV coverage radius with altitude [26], [39]. Thus, our analysis brings forth these new insights as it captures the relative effect of all four factors that impact the coverage radius concurrently: angular distance dependent realistic nonlinear antenna model, elevation angle dependent probability of LoS, shadowing, and a measurement backed path loss model.

3) *Height Versus Beamwidth:* There can be scenarios where height of UAV is subject to changes due to factors beyond the system designer's control such as weather, but the same coverage pattern has to be maintained. Our proposed model provides a mechanism to address such scenarios by characterizing the height versus beamwidth relationship, as shown in Fig. 5. For example, if a UAV is deployed to cover $r_f = 4000$ m with $\epsilon = 0.8$ at a height of 10 000 m and if its height is changed to 5000 m, the UAV will need to adjust its beamwidth from $70°$ to either $42°$ or $110°$ in order to continue providing the same coverage. Fig. 5 also highlights the importance of optimizing both beamwidth and height in tandem with each other rather than independently, as has been the case in prior works [16] and [39].
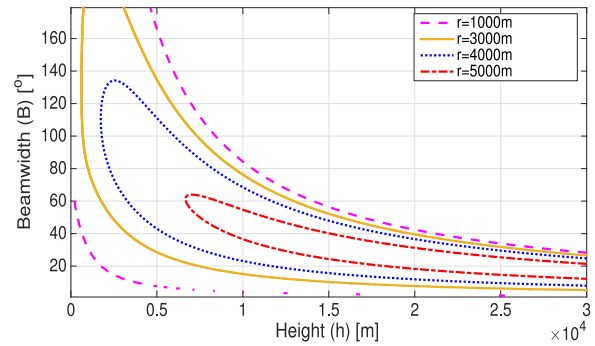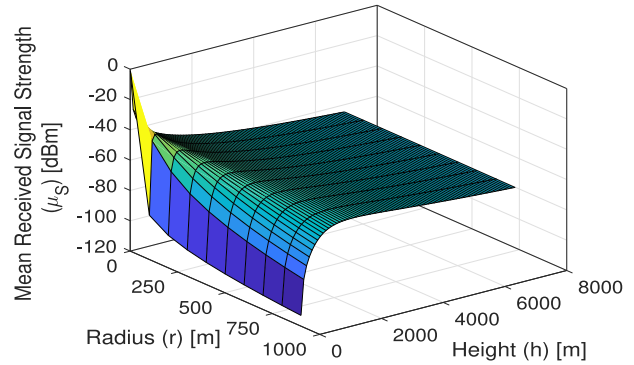

Fig. 6. Mean received signal with varying height for $B = 50°$.
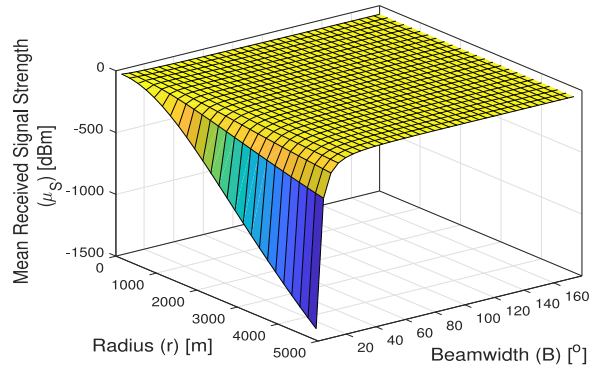

Fig. 7. Mean received signal with varying beamwidth at $h = 3500$ m.

B. Impact of Altitude, Beamwidth, and Radius on RSS

In order to investigate the behavior of RSS in context with UAV design parameters, Figs. 6 and 7 illustrate how the mean RSS varies with height and beamwidth with increasing cell radius r. In Fig. 6, mean RSS is plotted for $B = 50°$, $f = 2$ GHz, $P_t = 40$ dBm, and $\phi_{\text{tilt}} = 0°$ in a suburban environment. As expected, RSS decreases as r increases for any fixed height. However, for any r, RSS initially increases with height, reaches to a peak value, and then decreases as height increases further. The scenario in Fig. 7 consists of a UAV deployed at a height of 3500 m. Since a narrow beamwidth can only cover a small coverage area, the decrease in RSS with increasing radius is very rapid at low beamwidths. Hence, the trend of RSS with beamwidth is more clearly depicted in Fig. 8(a)–(c), which are zoomed-in plots of Fig. 7 for $20° \leq B < 180°$.
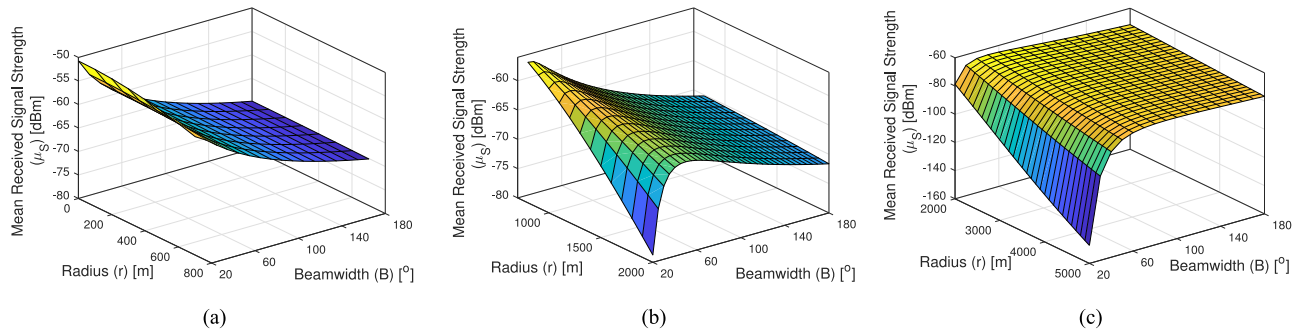
Fig. 8. Mean received signal on ground with varying beamwidths $> 20°$. (a) 0 m $< r <$ 800 m. (b) 800 m $< r <$ 2000 m. (c) 2000 m $< r <$ 5000 m.
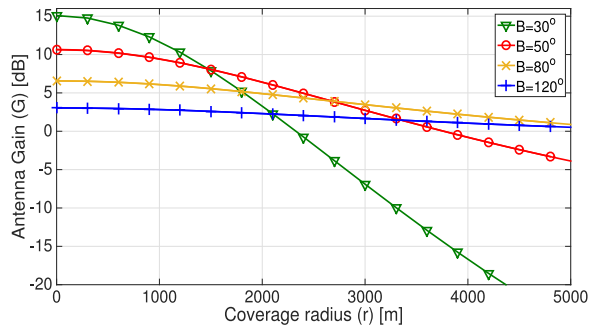

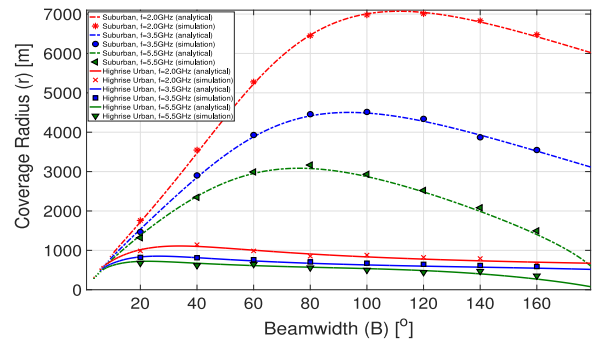Fig. 9. Antenna gain at $h = 3500$ m with varying radius for different beamwidths.

Fig. 10. Coverage radius against beamwidth for varying frequency and environment at $h = 3000$ m.

The continuous decrease of coverage radius with increase in beamwidth for $r <$ 800 m in Fig. 8(a) can be attributed to the continuous decrease of antenna gain with radius in Fig. 9 for $r <$ 800 m. As we approach closer to 1000 m, the trend in antenna gain pattern starts to reverse for different beamwidths, and we observe several intersecting points from $1000 < r < 2500$ in Fig. 9, and hence, mean RSS in Fig. 8(b) attains a parabolic shape with increasing beamwidth in this range. At very large r, antenna gain trend reverses completely and now it increases with increasing beamwidths, which is again in line with the RSS trend in Fig. 8(c).

Also note that at very large coverage radius, for example, at $r = 4000$ m in Fig. 8(c), RSS decreases very sharply from $50°$ to $30°$ as compared to decrease in RSS from $120°$ to $80°$. This is because at 4000 m in Fig. 9, difference in gain between $50°$ and $30°$ is quite high as compared to difference in gain between $120°$ and $80°$.

C. Analysis for Different Frequencies and Environments

In Fig. 10, we quantify the tradeoff of coverage radius with beamwidth in changing environments and at different frequencies. The figure is plotted for $h = 3000$ m, $PL_{max} = 120$ dB for two extreme environments, suburban, and high-rise urban. From Fig. 10, we observe that in addition to coverage radius decreasing sharply as frequency increases or environment becomes denser, the beamwidth at which this coverage radius versus beamwidth trend changes is also lower in a more denser environment or at a higher

frequency. For example, in high-rise urban environment, decrease in radius starts from a beamwidth of as low as $30°$ at 2.0 GHz, whereas for the same frequency, this decrease does not start until $110°$ in case of the suburban environment. Similar observations can be made by observing the effect of frequency in the same environment. This is not just because of free space path loss that increases with increasing frequency, but also because of shadowing, which increases at higher frequencies for the same environment [45]. In addition, the impact of frequency on coverage radius reduces as environment becomes denser. These observations could play a valuable role for designing UAV-based cellular systems at higher frequencies by utilizing the unused part of higher frequency spectrum such as mmWave. The analytical results are also corroborated with simulation results in Fig. 10.

D. Validation of Analysis With Monte Carlo Simulations

The tradeoffs between coverage radius, beamwidth, and height presented in the preceding sections have already been verified through Monte Carlo simulations, as shown in Figs. 4 and 10. Next, we corroborate the results derived for the RSS model in (17)–(19) via simulations. Figs. 11 and 12 show PDF of RSS at two arbitrary points, located at $r = 3000$ m for UAVs deployed at height of $h = 2000$ m and beamwidths of $B = 5°$ and $50°$, respectively. The RSS PDF obtained from our derived analytical expression in (18) shows an excellent fit to simulation based RSS data. In Fig. 11, users located at $r = 3000$ m receive extremely
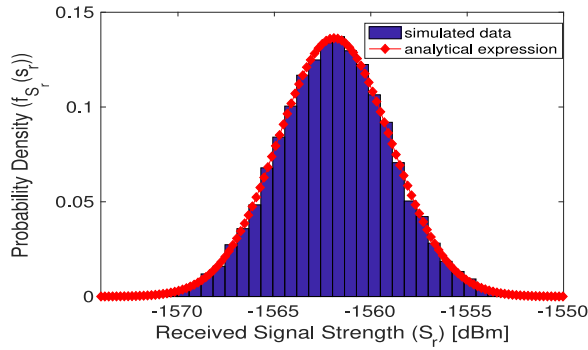
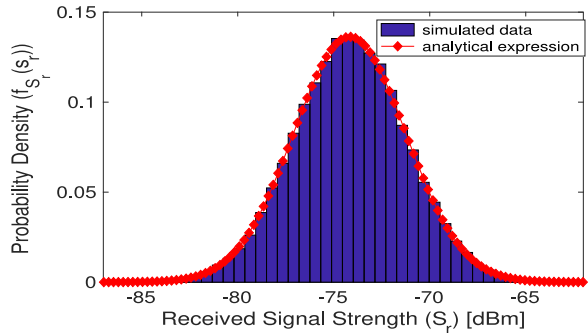Fig. 11. PDF of RSS at $r = 3000$ m, $B = 5°$ and $h = 2000$ m.

Fig. 12. PDF of RSS at $r = 3000$ m, $B = 50°$ and $h = 2000$ m.

low RSS since a small beamwidth of $5°$ can cover only a small area. In contrast, when beamwidth is increased to $50°$, the same users start to receive a much better coverage, i.e., between -85 to -65 dBm.

We now extend our analysis from RSS at any arbitrary point to RSS inside a geographical area of 8000 m $\times$ 8000 m. Normalized histograms of RSS from the simulation results and analytical PDFs from (19) are in agreement, as shown in Figs. 13 and 14. From Figs. 13 and 14, we note that not only the range of RSS becomes narrower in a given area, but also the distribution of RSS approaches zero skewed Gaussian with either increasing height or increasing beamwidth.

E. Comparison of Altitude and Beamwidth to Control Coverage

Noting that both beamwidth and height can be used for the same purpose of controlling coverage leads us toward comparing both of these parameters by analyzing the sensitivity of coverage radius to each of these parameters.

Figs. 15 and 16 show the gradient of radius with respect to beamwidth obtained by differentiating (15) with respect to beamwidth or determining gradient of the curves in Fig. 3 with respect to beamwidth. By comparing the absolute values of $\Delta r / \Delta B$ in Figs. 15 and 16, we conclude that the change in coverage radius is most sensitive to very high heights (up to 25000 m).

Next, we analyze the rate of change of radius with height ($\Delta r / \Delta h$) in Fig. 17. Unlike Fig. 15, the values of derivatives here follow a similar pattern with changing beamwidths except for beamwidths $< 25°$ where $\Delta r / \Delta h$ is constant. By comparing values of the derivative in Fig. 17 with Figs. 15

and 16 (both comparisons range from samples of heights from 0 to 25000 m and beamwidths from $1°$ to $180°$), we note that $\max(\Delta r / \Delta B) >> \max(\Delta r / \Delta h)$. Numerically, the maximum value of $\max(\Delta r / \Delta B)$, -2000, is almost 75 times greater than the maximum value of $\max(\Delta r / \Delta h)$, -27.

This indicates that low beamwidths lead to greatest change (decrease) in coverage radius per unit beamwidth as compared to change in radius per unit height. This analysis can be leveraged to choose between the height and beamwidth or design appropriate combination of the two for optimizing coverage.

F. Coverage Probability With Varying Tilt Angles and Asymmetric Beamwidths

Coverage analysis of scenarios with varying tilt angles and asymmetrical beamwidths is presented in this section. In Fig. 18, we compare the probability of coverage using zero antenna tilt with a tilt angle of $10°$. For nonzero tilt angles, the coverage pattern forms an off-centered ellipse shape rather than a circle centered at the origin. The coverage probability in case of nonzero tilt angle is evaluated by using (13). Fig. 19 shows how the coverage probability changes with different values of B_ϕ and B_θ. The effect of changing tilt values is depicted in Fig. 20. It is observed that although a UAV with antenna tilt of $80°$ covers more area as compared to tilt angle of $20°$, the maximum coverage probability with $\phi_{\text{tilt}} = 80°$ is reduced by half as compared to $\phi_{\text{tilt}} = 20°$. These figures highlight the capability of our derived equations and the underlying system model to extend the analysis to a wide range of scenarios, such as nonzero tilt angle and asymmetrical beamwidths. Complete analysis of UAV system design in such extended scenarios to provide an even more flexible and on-demand cellular coverage can be focus of a future study.

G. Coverage Analysis With Multiple UAVs

Previous literature [39] utilizes circle packing theory to determine the number of UAVs to achieve a gain in coverage probability in a certain geographical area. In the circle packing problem, N identical circles (cells) are arranged inside a larger circle (target area) of radius R_t such that the packing density is maximized and none of the circles overlap [46]. The radius of each of the N circles that solves this problem is denoted by $r_{\max}$ and one UAV provides coverage to one small cell (circle). However, this approach toward determining the needed number of UAVs for achieving a coverage level has two major drawbacks. First, significant gaps between circles or cells are inevitable when two or more circles are used to cover a given area. This is due to the inherent nature of circle packing theory, since in order to cover the target area completely, $N \to \infty$ and $r_{\max} \to 0$. Second, the number of circles (UAVs) increase rapidly with desired coverage probability. We overcome both of these problems by introducing a UAV placement model that simply uses hexagonal cell shapes instead of circle. This approach not
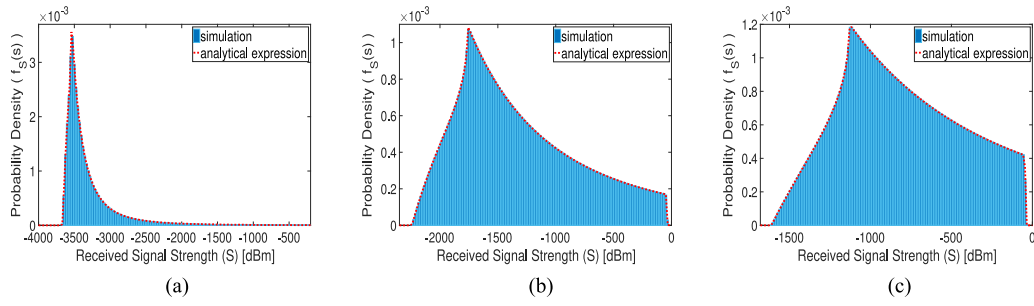
Fig. 13. PDF of RSS on ground with changing altitude of UAV for $B = 5°$. (a) $h = 500$ m. (b) $h = 3500$ m. (c) $h = 5500$ m.
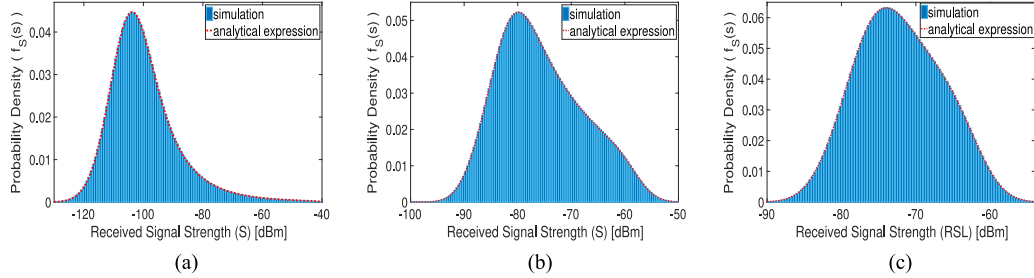

Fig. 14. PDF of RSS on ground with changing altitude of UAV for $B = 50°$. (a) $h = 500$ m. (b) $h = 3500$ m (c) $h = 5500$ m.
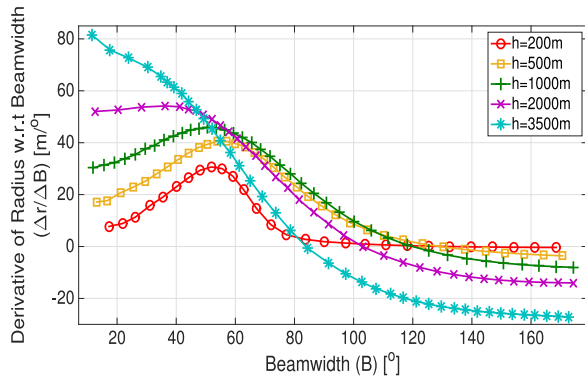

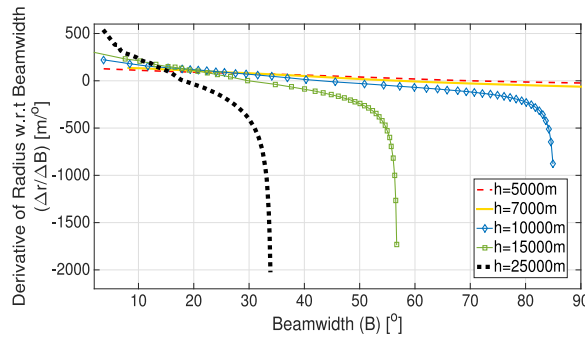Fig. 15. Gradient of coverage radius with respect to beamwidth.

Fig. 16. Gradient of coverage radius with respect to beamwidth for different heights in low beamwidth regime.

only resolves aforementioned problems but also leads to a better coverage. To illustrate our approach, consider the case for $N = 3$ in Fig. 21. If we consider a hexagonal area with the longest distance from center to the edge denoted by R_t and the distance from center, to the vertex of a hexagon

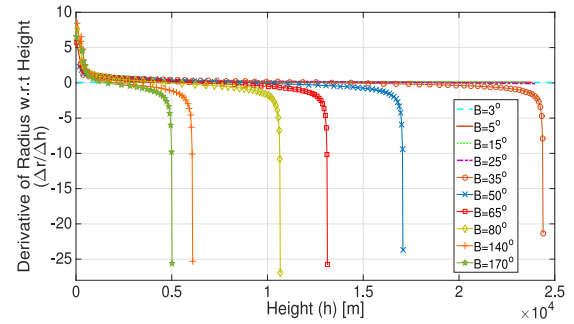Fig. 17. Gradient of coverage radius with respect to height.
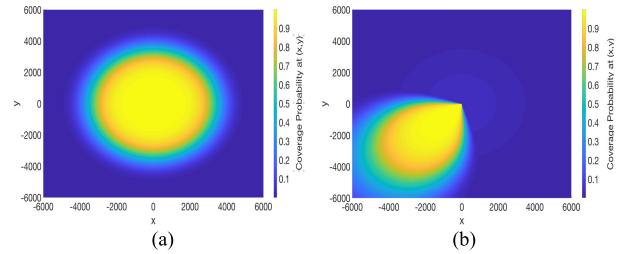

Fig. 18. Coverage probability at $B = 50°$ and $h = 5000$ m. (a) $\phi_{\text{tilt}} = 0°$. (b) $\phi_{\text{tilt}} = 10°$ and $\theta_a = 45°$.
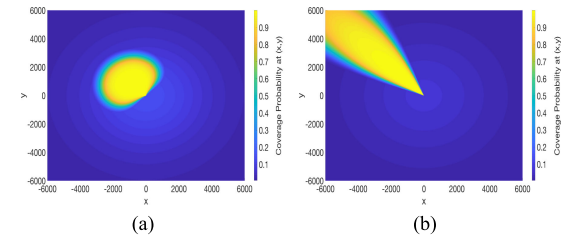

Fig. 19. Coverage probability with asymmetrical beamwidths at $\phi_{\text{tilt}} = 10°$, $\theta_a = -45°$, and $h = 5000$ m. (a) $B_\phi = 20°$ and $B_\theta = 70°$. (b) $B_\phi = 70°$ and $B_\theta = 20°$.
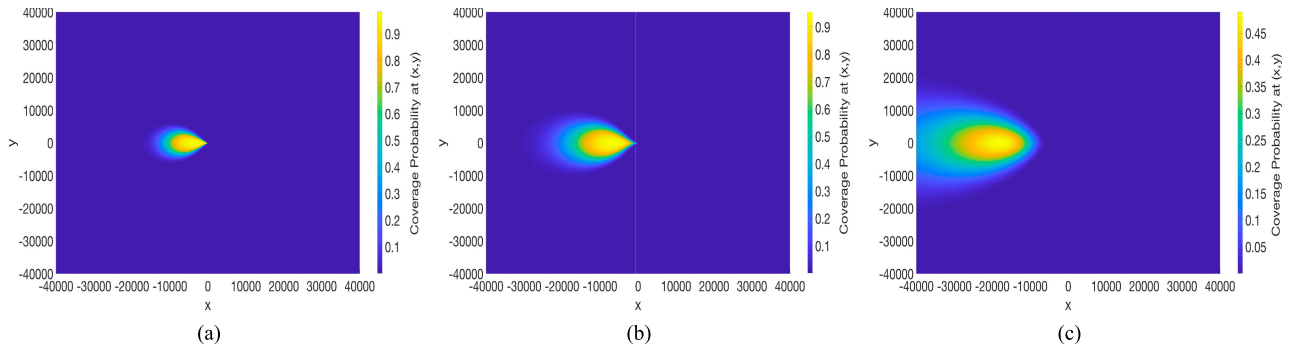
Fig. 20.   Coverage probability with varying tilt angles at $B = 40°$ and $h = 10000$ m. (a) $\phi_{\text{tilt}} = 20°$. (b) $\phi_{\text{tilt}} = 40°$. (c) $\phi_{\text{tilt}} = 80°$.
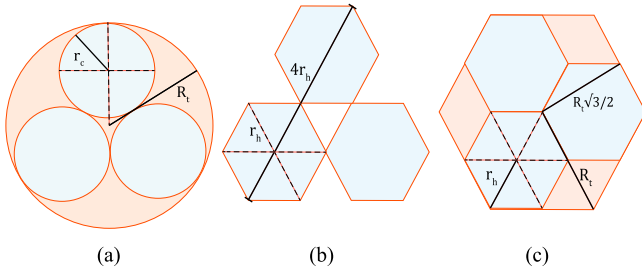

Fig. 21.   Circle packing versus hexagonal packing for $N = 3$. (a) Circle packing. (b) Maximum distance between hexagons. (c) Hexagon packing.

by r_h, then the maximum distance between any two farthest hexagons will be $4r_h$, as shown in Fig. 21(b). Our goal is to minimize this distance in order to maximize the packing density, thus leading to the arrangement shown in Fig. 21(c). Here, the maximum distance between farthest hexagons is $4r_h\sqrt{3}/2 < 4r_h$, leading to $r_h = 0.5R_t = r_{\max}$. The maximum total coverage (in percentage) for $N = 3$ can then be calculated as follows:

$$C_h = \frac{\text{area covered by three UAVs}}{\text{total area to be covered}} = \frac{3\left(\frac{3}{2}\sqrt{3}\left(\frac{1}{2}R_t\right)^2\right)}{\frac{3}{2}\sqrt{3}R_t^2}$$
$$= 75\%. \qquad (21)$$

Similar analysis is done for $N = 1$ to 10 and presented in Table IV, where C_c and C_h represent the maximum percentage of actual area covered out of total target area using circular and hexagonal packing, respectively, whereas $r_{\max}^c$ and $r_{\max}^h$ represent the maximum possible radius of each cell using the two approaches. We compare the results of our proposed approach with those from [39] that utilizes circle packing to the same effect. From our proposed approach, the minimum possible coverage is ~70% for any number of UAVs, whereas with circle packing theory it drops to as low as 50% [39]. This has a direct impact on the coverage threshold requirement of the system. It is highlighted in [39] that a 0.7 coverage performance is impossible to achieve with $1 < N < 7$ using circle packing approach. Our proposed hexagonal packing strategy, on the other hand, ensures that this coverage performance demand can be met with much smaller number of UAVs. We illustrate this by calculating the minimum number of UAVs required to cover differ-

TABLE IV
Comparison Between Circular and Hexagonal Packing in Terms
of Coverage Radius of Each UAV and Maximum Total Coverage

N	r_{max}^c from [39]	r_{max}^h	C_c from [39]	C_h
1	R_t	R_t	1	1
2	$0.500R_t$	$0.447R_t$	50.0	75.0
3	$0.464R_t$	$0.500R_t$	64.6	75.0
4	$0.413R_t$	$0.400R_t$	68.6	75.0
5	$0.370R_t$	$0.333R_t$	68.5	75.0
6	$0.333R_t$	$0.286R_t$	66.6	75.0
7	$0.333R_t$	$0.333R_t$	77.8	77.8
8	$0.302R_t$	$0.286R_t$	73.3	72.7
9	$0.275R_t$	$0.250R_t$	68.9	69.2
10	$0.261R_t$	$0.286R_t$	68.7	75.0
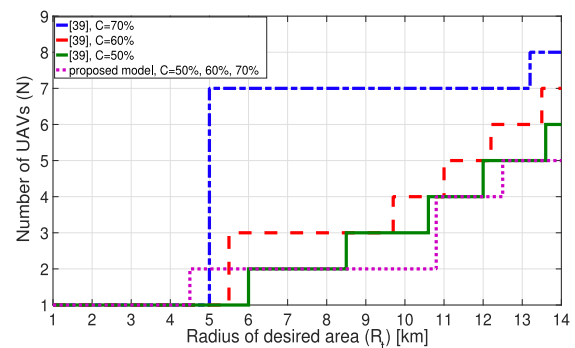
Fig. 22.   Minimum number of UAVs versus radius of desired area for different minimum coverage thresholds.

ent geographical areas by utilizing Table IV for a coverage threshold $\geq 70\%$, with a tolerance of $\pm1\%$ for $\epsilon = 0.8$ over $0 < h \leq 5000$ and $1 < B < 180$. Fig. 22 compares the resulting minimum number of UAVs obtained with hexagonal packing and circle packing from [39]. For $C = 70\%$, from circle packing approach, we can cover a desired area up to 14 km with one, seven, or eight UAVs. On the other hand, with our proposed hexagonal packing approach, we can cover an area with a much smaller number of UAVs, i.e., one, two, four, or five UAVs. However, the number of UAVs required to serve multiple users would also depend

Fig. 23. Optimal beamwidth for multiple UAVs and corresponding radius of each UAV.

Fig. 24. Altitude with varying number of UAVs for different beamwidths.

on transmit power and bandwidth allocation of multiple UAVs. Such considerations are not a focus of this paper. The reader is referred to three excellent works that deal with maximizing the minimum average rate of users via joint bandwidth and transmit power allocation [13], [31], [36] for detailed insight into these considerations.
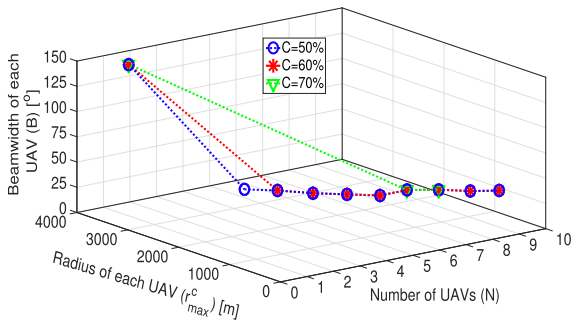
Another advantage that hexagonal packing offers is the relative scalability of number of UAVs as the coverage threshold changes, which in case of circle packing increases rapidly as coverage threshold goes from 50% to 80%, as shown in Fig. 22.

Next, we investigate the relationship between number of UAVs and beamwidth of each UAV. First, we find the maximum possible r for a given geographical area with radius R_t using Table IV as the number of UAVs vary and then the corresponding beamwidth using Fig. 3 from our proposed model. Fig. 23 illustrates the results for a UAV deployed at a height of 1000 m to cover a target geographical area of $R_t = 3500$ m in a suburban environment. The overall decreasing trend between beamwidth and number of UAVs for different coverage requirements quantifies the intuitive observation that we can either cover the same area with a single UAV having a wide beamwidth or with multiple UAVs having narrow beamwidths. For example, for a coverage threshold of 60%, a target area of radius 3500 m can be covered either with ten UAVs, each having a beamwidth of 22° or with a single UAV having a beamwidth of 150°. Thus proposed model enables more design options for a wireless system designer with regards to conservation of infrastructure.

Finally, in order to observe the trend of UAV altitude as the number of UAVs varies, the optimal UAV altitude that yields maximum possible coverage is plotted in Fig. 24 for different number of UAVs. The system model using binary antenna gain pattern proposed in earlier studies, such as [39], does not reflect the role of beamwidth in UAV altitude with increasing number of UAVs. Hence, UAV altitude decreases monotonically as number of UAVs increases. Fig. 24 shows that this is not the case when a practical antenna gain pattern, as proposed in this study, is used. In the plot, one UAV covers maximum possible area for a certain beamwidth that can be found from Fig. 4. For beamwidths up to 15°, UAV altitude with number of UAVs follows the same trend as in [39]. However, the trend changes for higher beamwidths. This trend is explicitly compared with
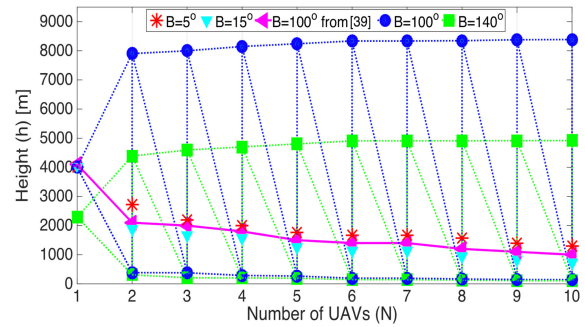
the model in [39] for a beamwidth of 100°. This concludes that, contrary to observation made in prior studies with simple or no antenna models, it is not necessary for UAV altitude to decrease monotonically as the number of UAV increases; in fact, it can also either increase monotonically or behave as a combination of increasing and decreasing altitude as the number of UAVs increase.

Presented analysis can also be exploited for interference management in the presence of other aerial platforms since it provides multiple altitude options for UAV deployment, thus leading to more flexible design options, which is imperative to the design of next generation cellular systems. Such investigations of interference using the proposed model can be focus of a future study. Note that in order to provide full coverage of the considered area, significant overlaps will be inevitable. Several techniques can be leveraged to optimize the number of UAVs needed for full coverage, for example, [47] minimizes the number of UAVs needed to provide wireless coverage for a group of distributed ground terminals, ensuring that each ground termination is within the communication range of at least one UAV. The work in [47] analyzes the UAV placement problem under LoS conditions without antenna model considerations and can be extended to incorporate other elevation angle dependent factors considered in this study. Determining the optimal overlap can be handled using techniques, such as adaptive bandwidth allocation among the UAVs as proposed in future work of [36].

For discussions related to other UAV deployment challenges, such as battery considerations, limited payload capacity, security, and hostile weather conditions, the reader is referred to [2] and [48].

V. CONCLUSION

This paper provides a holistic analysis of the interplay between key UAV deployment parameters: coverage radius, height, and beamwidth while considering design space dimensions that remain unexplored in existing studies. It further provides a mathematical model to estimate RSS at any distance from boresight of antenna as a function of antenna beamwidth and altitude. The analysis and results provide several new insights that prior models with no or simplified antenna, path loss, or shadowing models do not reveal, which are as follows.

1) UAV altitude or antenna beamwidth does not have to necessarily increase continuously for higher coverage radius.
2) Contrary to findings reported in some prior studies, UAV coverage radius does not necessarily increase as altitude increases.
3) The minimum number of UAVs required to cover a given area does not necessarily decrease monotonically as UAV altitude increases.

These results allow us to determine optimal UAV parameters for realistic deployment.

Furthermore, based on the analysis of effect of beamwidth and altitude on coverage radius, it is found that antenna beamwidth and altitude should be optimized simultaneously rather than independently, as is the case assumed in previous works. It is also concluded that optimizing beamwidth instead of height to control coverage may be more practical and that coverage is most sensitive to beamwidths of less than $40°$.

A hexagonal packing is proposed for solving coverage optimization problem with multiple UAVs. The advantage of proposed scheme is that it leaves much smaller coverage holes. Thus, it can cover a higher proportion of the given area with same number of UAVs compared to circle packing and is scalable in terms of number of UAVs with increasing probability of coverage.

APPENDIX

The PDF of RSS at an arbitrary point in a cell is found by first deriving PDFs of received signal strengths in LoS and NLoS scenarios using transformations of RVs. Thereafter, the theorem for finding PDF of sums of independent RVs from [49] is applied.

For the scenario with circular coverage pattern of the UAV, we can express the RV $S_l(h, r, B)$ from (17) as follows:

$$S_l(h, r, B) = P_l(\phi_{\mathrm{MS}})R_l(h, r, B)$$

$$= P_l(\phi_{\mathrm{MS}})\left[10\log\left(\frac{29000}{B^2}\right) - 12\left(\frac{\tan^{-1}\left(\frac{r}{h}\right) - \phi_{\mathrm{tilt}}}{B}\right)^2\right.$$

$$\left. + T - 20\log\left(\frac{4\pi f d}{c}\right)\right] - P_l(\phi_{\mathrm{MS}})X_l$$

$$= P_l(\phi_{\mathrm{MS}})A_1 - P_l(\phi_{\mathrm{MS}})X_l \qquad (22)$$

where P_l is given in (2) and A_1 can be treated as a constant for a UAV deployed at a fixed height and beamwidth, as given by

$$A_1 = T + 10\log\left(\frac{29000}{B^2}\right) - 12\left(\frac{\tan^{-1}\left(\frac{r}{h}\right) - \phi_{\mathrm{tilt}}}{B}\right)^2$$

$$- 20\log\left(\frac{4\pi f d}{c}\right). \qquad (23)$$

We proceed by first finding PDF of S_l by applying transformations of RVs as follows:

$$F_{S_l}(s_l) = \mathrm{P}\,(S_l \leq s_l)$$

$$= \mathrm{P}\,(P_l(\phi_{\mathrm{MS}})A_1 - P_l(\phi_{\mathrm{MS}})X_l \leq s_l)$$

$$= \mathrm{P}\left(X_l \leq \frac{s_l - P_l(\phi_{\mathrm{MS}})A_1}{P_l(\phi_{\mathrm{MS}})}\right)$$

$$F_{S_l}(s_l) = F_{X_l}\left(\frac{s_l - P_l(\phi_{\mathrm{MS}})A_1}{P_l(\phi_{\mathrm{MS}})}\right) \qquad (24)$$

where $F_{S_l}(s_l)$ and $F_{X_l}(x_l)$ are the CDFs of S_l and X_l, respectively. Note that P_l is a function of ϕ_{MS}, which is in turn a function of h and r. However, for compactness, this dependence is omitted in subsequent analysis.

Both sides of (24) are a function of s_l, and therefore, we differentiate both sides w.r.t. s_l in order to get the PDF

$$f_{S_l}(s_l) = f_{X_l}\left(\frac{s_l - P_l A_1}{P_l}\right)\frac{d}{ds_l}\left(\frac{s_l - P_l A_1}{P_l}\right)$$

$$f_{S_l}(s_l) = \frac{1}{P_l}f_{X_l}\left(\frac{s_l - P_l A_1}{P_l}\right). \qquad (25)$$

This allows us to find the PDF of S_l based on the PDF of X_l, which is $\mathcal{N}(0, \sigma_n)$ RV. Applying the transformation in (25) yields the following expression for $f_{S_l}(s_l)$:

$$f_{S_l}(s_l) = \frac{\exp\left(-\frac{(s_l - P_l A_1)^2}{2(P_l \sigma_l)^2}\right)}{\sqrt{2\pi}\,P_l \sigma_l}. \qquad (26)$$

Following a similar procedure, we then derive PDF of S_n, which yields following expression:

$$f_{S_n}(s_n) = \frac{\exp\left(-\frac{(s_n - [P_n(A_1 - \mu_{\mathrm{sh}})])^2}{2(P_n)^2(\sigma_n^2 + \sigma_{\mathrm{sh}}^2)}\right)}{\sqrt{2\pi}\,P_n\sqrt{\sigma_n^2 + \sigma_{\mathrm{sh}}^2}}. \qquad (27)$$

We can now proceed to derive PDF of S_r by performing convolution of (26) with (27) as in (28) shown at the bottom of this page, where A_2 in (28) is expanded in (29) shown at the top of the next page.

$$f_{S_r}(s_r) = \int_{-\infty}^{\infty} \frac{1}{\sqrt{2\pi}\,P_n\sqrt{\sigma_n^2 + \sigma_{\mathrm{sh}}^2}}\exp\left[-\frac{(s_r - s_l - [P_n(A_1 - \mu_{\mathrm{sh}})])^2}{2(P_n)^2(\sigma_n^2 + \sigma_{\mathrm{sh}}^2)}\right]\frac{1}{\sqrt{2\pi}\,P_l\sigma_l}\exp\left[-\frac{(s_l - P_l A_1)^2}{2(P_l\sigma_l)^2}\right]ds_l$$

$$= \int_{-\infty}^{\infty} \frac{1}{\sqrt{2\pi}\sqrt{2\pi}\,P_n\sqrt{\sigma_n^2 + \sigma_{\mathrm{sh}}^2}\,P_l\sigma_l}\exp\left[-\frac{A_2}{2(P_l)^2\sigma_l^2(P_n)^2(\sigma_n^2 + \sigma_{\mathrm{sh}}^2)}\right]ds_l \qquad (28)$$

$$A_2 = (P_l)^2 \sigma_l^2 (s_r - s_l - [P_n (A_1 - \mu_{\text{sh}})])^2 + (P_n)^2 \left(\sigma_n^2 + \sigma_{\text{sh}}^2\right)(s_l - P_l A_1)^2$$

$$= (P_l)^2 \sigma_l^2 \left(s_r^2 + s_l^2 + [P_n (A_1 - \mu_{\text{sh}})]^2 - 2s_l s_r - 2s_r [P_n (A_1 - \mu_{\text{sh}})] + 2s_l [P_l (A_1 - \mu_{\text{sh}})]\right)$$

$$+ (P_n)^2 \left(\sigma_n^2 + \sigma_{\text{sh}}^2\right)\left(s_l^2 + (P_l A_1)^2 - 2s_l P_l A_1\right) \tag{29}$$

$$A_2 = s_l^2 \left[(P_l)^2 \sigma_l^2 + (P_n)^2 \left(\sigma_n^2 + \sigma_{\text{sh}}^2\right)\right] - 2s_l \left[(P_l \sigma_l)^2 (s_r - P_n(A_1 - \mu_{\text{sh}})) + (P_n)^2 \left(\sigma_n^2 + \sigma_{\text{sh}}^2\right) P_l A_1\right]$$

$$+ (P_l \sigma_l)^2 \left(s_r^2 + [P_n (A_1 - \mu_{\text{sh}})]^2 - 2s_r [P_n (A_1 - \mu_{\text{sh}})]\right) + (P_n)^2 \left(\sigma_n^2 + \sigma_{\text{sh}}^2\right) [P_l A_1]^2 \tag{30}$$

$$A_3 = s_l^2 - 2s_l \frac{\sigma_{s_l}^2 (s_r - [P_n (A_1 - \mu_{\text{sh}})]) + \sigma_{s_n}^2 P_l A_1}{\sigma_s^2} + \frac{\sigma_{s_l}^2 (s_r^2 + [P_n (A_1 - \mu_{\text{sh}})]^2 - 2s_r [P_n (A_1 - \mu_{\text{sh}})] + \sigma_{s_n} [P_l A_1]^2}{\sigma_s^2} \tag{33}$$

$$A_3 = \left(s_l - \frac{\sigma_{s_l}^2 (s_r - [P_n (A_1 - \mu_{\text{sh}})]) + \sigma_{s_n}^2 P_l A_1}{\sigma_s^2}\right)^2 - \left(\frac{\sigma_{s_l}^2 (s_r - [P_n (A_1 - \mu_{\text{sh}})]) + \sigma_{s_n}^2 P_l A_1}{\sigma_s^2}\right)^2$$

$$+ \left(\frac{\sigma_{s_l}^2 (s_r - [P_n (A_1 - \mu_{\text{sh}})])^2 + \sigma_{s_n}^2 P_l^2 A_1^2}{\sigma_s^2}\right) \tag{34}$$

$$f_{S_r}(s_r) = \frac{1}{\sqrt{2\pi}\sigma_s} \exp\left[-\frac{(s_r - [P_l A_1 + P_n (A_1 - \mu_{\text{sh}})])^2}{2\sigma_s^2}\right] \underbrace{\int_{-\infty}^{\infty} \frac{1}{\sqrt{2\pi}\frac{\sigma_{s_l}\sigma_{s_n}}{\sigma_s}} \exp\left[-\frac{s_l - \frac{\sigma_{s_l}^2(s_r - [P_n(A_1 - \mu_{\text{sh}})]) + \sigma_{s_n}^2 [P_l A_1]}{\sigma_s^2}}{2(\frac{\sigma_{s_l}\sigma_{s_n}}{\sigma_s})^2}\right] ds_l}_{=1} \tag{35}$$

Next, we perform algebraic manipulation on (29) in (30) shown at the top of this page, to convert the terms in it to $(C + D)^2$ form in order to apply completing the squares method. In order to complete the square of (30), we define a new variable in the following manner:

$$\sigma_s = \sqrt{\sigma_{s_l}^2 + \sigma_{s_n}^2} \tag{31}$$

where $\sigma_{s_l}^2 = (P_l \sigma_l)^2$ and $\sigma_{s_n}^2 = (P_n)^2 \left(\sigma_n^2 + \sigma_{\text{sh}}^2\right)$.

Therefore, our PDF expression in (28) reduces to

$$f_{S_r}(s_r) = \int_{-\infty}^{\infty} \frac{1}{\sqrt{2\pi}\sigma_s} \frac{1}{\sqrt{2\pi}\frac{\sigma_{s_l}\sigma_{s_n}}{\sigma_s}} \exp\left[-\frac{A_3}{2(\frac{\sigma_{s_l}\sigma_{s_n}}{\sigma_s})^2}\right] \tag{32}$$

where A_3 is equal to (33) shown at the top of this page.

Squares are now completed by collecting the appropriate terms as in (34) shown at the top of this page. Finally, the exponent in (32) can be broken into a product of two exponents, as shown in (35) at the top of this page. By noting that the integral in (35) is in fact a Gaussian distribution on S_l (and hence integrates to 1), substituting σ_s from (31), P_l and P_n from (2) lead to the expression of PDF of S_r in (18).

ACKNOWLEDGMENT

REFERENCES

[1] A. Imran and R. Tafazolli
Performance & capacity of mobile broadband WiMAX (802.16e) deployed via high altitude platform
In *Proc. IEEE Eur. Wireless Conf.*, 2009, pp. 319–323.

[2] Y. Zeng, R. Zhang, and T. J. Lim
Wireless communications with unmanned aerial vehicles: Opportunities and challenges
IEEE Commun. Mag., vol. 54, no. 5, pp. 36–42, May 2016.

[3] Y. Mao, Y. Luo, J. Zhang, and K. B. Letaief
Energy harvesting small cell networks: Feasibility, deployment, and operation
IEEE Commun. Mag., vol. 53, no. 6, pp. 94–101, Jun. 2015.

[4] G. Maral and M. Bousquet
Satellite Communications Systems: Systems, Techniques and Technology. Hoboken, NJ, USA: Wiley, 2011.

[5] K. Gomez, T. Rasheed, L. Reynaud, and S. Kandeepan
On the performance of aerial LTE base-stations for public safety and emergency recovery
In *Proc. IEEE Globecom Workshops*, 2013, pp. 1391–1396.

[6] Z. Shao, Y. Liu, Y. Wu, and L. Shen
A rapid and reliable disaster emergency mobile communication system via aerial ad hoc BS networks
In *Proc. 7th Int. Conf. Wireless Commun., Netw. Mobile Comput.*, 2011, pp. 1–4.

[7] W. H. Robinson and A. P. Lauf
Resilient and efficient MANET aerial communications for search and rescue applications
In *Proc. Int. Conf. Comput., Netw., Commun.*, 2013, pp. 845–849.

[8] S. Kandeepan, K. Gomez, L. Reynaud, and T. Rasheed
Aerial-terrestrial communications: terrestrial cooperation and energy-efficient transmissions to aerial base stations
IEEE Trans. Aerosp. Electron. Syst., vol. 50, no. 4, pp. 2715–2735, Oct. 2014.

[9] J. Lyu, Y. Zeng, and R. Zhang
     UAV-aided offloading for cellular hotspot
     IEEE Trans. Wireless Commun., vol. 17, no. 6, pp. 3988–4001,
     Jun. 2018.

[10] A. Imran, M. Shateri, and R. Tafazolli
     On the comparison of performance, capacity and economics of
     terrestrial base station and high altitude platform based deploy-
     ment of 4G
     In *Proc. 6th ACM Symp. Perform. Eval. Wireless Ad Hoc, Sen-
     sor, Ubiquitous Netw.*, 2009, pp. 58–62.

[11] S. Rohde and C. Wietfeld
     Interference aware positioning of aerial relays for cell overload
     and outage compensation
     In *Proc. IEEE Veh. Technol. Conf.*, 2012, pp. 1–5.

[12] D. Grace, J. Thornton, G. Chen, G. P. White, and T. C. Tozer
     Improving the system capacity of broadband services using
     multiple high-altitude platforms
     IEEE Trans. Wireless Commun., vol. 4, no. 2, pp. 700–709,
     Mar. 2005.

[13] J. Lyu, Y. Zeng, and R. Zhang
     Spectrum sharing and cyclical multiple access in UAV-aided
     cellular offloading
     In *Proc. IEEE Global Commun. Conf.*, Dec. 2017, pp. 1–6.

[14] N. H. Motlagh, T. Taleb, and O. Arouk
     Low-altitude unmanned aerial vehicles-based internet of
     things services: Comprehensive survey and future perspec-
     tives
     IEEE Internet Things J., vol. 3, no. 6, pp. 899–922,
     Dec. 2016.

[15] C. Zhan, Y. Zeng, and R. Zhang
     Energy-efficient data collection in UAV enabled wireless sen-
     sor network
     IEEE Wireless Commun. Lett., vol. 7, no. 3, pp. 328–331,
     Jun. 2018.

[16] A. Al-Hourani, S. Kandeepan, and S. Lardner
     Optimal LAP altitude for maximum coverage
     IEEE Wireless Commun. Lett., vol. 3, no. 6, pp. 569–572,
     Dec. 2014.

[17] A. Al-Hourani, S. Chandrasekharan, G. Kaandorp, W. Glenn, A.
     Jamalipour, and S. Kandeepan
     Coverage and rate analysis of aerial base stations
     IEEE Trans. Aerosp. Electron. Syst., vol. 52, no. 6, pp. 3077–
     3081, Dec. 2016.

[18] M. Mozaffari, W. Saad, M. Bennis, and M. Debbah
     Drone small cells in the clouds: Design, deployment and per-
     formance analysis
     In *Proc. IEEE Global Commun. Conf.*, 2015, pp. 1–6.

[19] F. Qixing, J. McGeehan, E. K. Tameh, and A. R. Nix
     Path loss models for air-to-ground radio channels in urban
     environments
     In *Proc. IEEE 63rd Veh. Technol. Conf.*, 2006, vol. 6, pp. 2901–
     2905.

[20] M. Mozaffari, W. Saad, M. Bennis, and M. Debbah
     Unmanned aerial vehicle with underlaid device-to-device com-
     munications: Performance and tradeoffs
     IEEE Trans. Wireless Commun., vol. 15, no. 6, pp. 3949–3963,
     Jun. 2016.

[21] J. Thornton, D. Grace, M. H. Capstick, and T. C. Tozer
     Optimizing an array of antennas for cellular coverage from a
     high altitude platform
     IEEE Trans. Wireless Commun., vol. 2, no. 3, pp. 484–492,
     May 2003.

[22] J. Thornton and D. Grace
     Effect of lateral displacement of a high-altitude platform on
     cellular interference and handover
     IEEE Trans. Wireless Commun., vol. 4, no. 4, pp. 1483–1490,
     Jul. 2005.

[23] N. Goddemeier, K. Daniel, and C. Wietfeld
     Coverage evaluation of wireless networks for unmanned aerial
     systems
     In *Proc. IEEE Globecom Workshops*, Dec. 2010, pp. 1760–
     1765.

[24] S. T. G. Maguire and P. A. Robertson
     UAV attitude estimation using low-frequency radio polarization
     measurements
     IEEE Trans. Aerosp. Electron. Syst., vol. 53, no. 1, pp. 2–11,
     Feb. 2017.

[25] A. Mahmood, J. W. Wallace, and M. A. Jensen
     UAV attitude estimation using antenna arrays
     In *Proc. IEEE Int. Symp. Antennas Propag. USNC/URSI Nat.
     Radio Sci. Meeting*, Jul. 2017, pp. 1863–1864.

[26] J. Komerl and A. Vilhar
     Base stations placement optimization in wireless networks for
     emergency communications
     In *Proc. IEEE Int. Conf. Commun. Workshops*, 2014, pp. 200–
     205.

[27] R. I. Bor-Yaliniz, A. El-Keyi, and H. Yanikomeroglu
     Efficient 3-D placement of an aerial base station in next gener-
     ation cellular networks
     In *Proc. IEEE Int. Conf. Commun.*, 2016, pp. 1–5.

[28] A. Al-Hourani and S. Kandeepan
     Cognitive relay nodes for airborne LTE emergency networks
     In *Proc. 7th Int. Conf. Signal Process. Commun. Syst.*, 2013,
     pp. 1–9.

[29] Y. Zeng and R. Zhang
     Energy-efficient UAV communication with trajectory optimiza-
     tion
     IEEE Trans. Wireless Commun., vol. 16, no. 6, pp. 3747–3760,
     Jun. 2017.

[30] Y. Zeng, X. Xu, and R. Zhang
     Trajectory design for completion time minimization in UAV-
     enabled multicasting
     IEEE Trans. Wireless Commun., vol. 17, no. 4, pp. 2233–2246,
     Apr. 2018.

[31] Q. Wu, Y. Zeng, and R. Zhang
     Joint trajectory and communication design for multi-UAV en-
     abled wireless networks
     IEEE Trans. Wireless Commun., vol. 17, no. 3, pp. 2109–2121,
     Mar. 2018.

[32] D. Yang, Q. Wu, Y. Zeng, and R. Zhang
     Energy trade-off in ground-to-UAV communication via trajec-
     tory design
     IEEE Trans. Veh. Technol., vol. 67, no. 7, pp. 6721–6726,
     Jul. 2018.

[33] J. Lyu, Y. Zeng, and R. Zhang
     Cyclical multiple access in UAV-aided communications: A
     throughput-delay tradeoff
     IEEE Wireless Commun. Lett., vol. 5, no. 6, pp. 600–603,
     Dec. 2016.

[34] P. Zhan, K. Yu, and A. L. Swindlehurst
     Wireless relay communications with unmanned aerial vehicles:
     Performance and optimization
     IEEE Trans. Aerosp. Electron. Syst., vol. 47, no. 3, pp. 2068–
     2085, Jul. 2011.

[35] D. H. Choi, S. H. Kim, and D. K. Sung
     Energy-efficient maneuvering and communication of a single
     UAV-based relay
     IEEE Trans. Aerosp. Electron. Syst., vol. 50, no. 3, pp. 2320–
     2327, Jul. 2014.

[36] Y. Zeng, R. Zhang, and T. J. Lim
     Throughput maximization for UAV-enabled mobile relaying
     systems
     IEEE Trans. Commun., vol. 64, no. 12, pp. 4983–4996,
     Dec. 2016.

[37] J. Holis, D. Grace, and P. Pechac
Effect of antenna power roll-off on the performance of 3G cellular systems from high altitude platforms
IEEE Trans. Aerosp. Electron. Syst., vol. 46, no. 3, pp. 1468–1477, Jul. 2010.

[38] H. He, S. Zhang, Y. Zeng, and R. Zhang
Joint altitude and beamwidth optimization for UAV-enabled multiuser communications
IEEE Commun. Lett., vol. 22, no. 2, pp. 344–347, Feb. 2018.

[39] M. Mozaffari, W. Saad, M. Bennis, and M. Debbah
Efficient deployment of multiple unmanned aerial vehicles for optimal wireless coverage
IEEE Commun. Lett., vol. 20, no. 8, pp. 1647–1650, Aug. 2016.

[40] *Unmanned Systems Antennas Airborne Platforms, UAVs, Ground Vehicles, Robots*, UMS Antennas Issue 3, Cobham Antenna Systems, European Antennas, Ltd., Cheveley, U.K., 2010.

[41] A. Rocha, A. M. Correia, H. Adeli, R. L. Paulo, and S. Costanzo
Recent Advances in Information Systems and Technologies, vol. 3. Berlin, Germany: Springer, 2017, pp. 557–558.

[42] "Further advancements for E-UTRA physical layers aspects (release 9)
3rd Gener. Partnership Project, Sophia Antipolis, France, Tech. Rep. TR36.814 v9.0.0, Mar. 2010.

[43] C. A. Balanis
Antenna Theory: Analysis and Design. Hoboken, NJ, USA: Wiley, 2016.

[44] Q. Feng, E. K. Tameh, A. R. Nix, and J. McGeehan
Modelling the likelihood of line-of-sight for air-to-ground radio propagation in urban environments
In *Proc. IEEE Globecom*, 2006, pp. 1–5.

[45] J. Holis and P. Pechac
Elevation dependent shadowing model for mobile communications via high altitude platforms in built-up areas
IEEE Trans. Antennas Propag., vol. 56, no. 4, pp. 1078–1084, Apr. 2008.

[46] Z. Gspr and T. Tarnai
Upper bound of density for packing of equal circles in special domains in the plane
Periodica Polytechnica Civil Eng., vol. 44, no. 1, pp. 13–32, 2000.

[47] J. Lyu, Y. Zeng, R. Zhang, and T. J. Lim
Placement optimization of UAV-mounted mobile base stations
IEEE Commun. Lett., vol. 21, no. 3, pp. 604–607, Mar. 2017.

[48] L. Gupta, R. Jain, and G. Vaszkun
Survey of important issues in UAV communication networks
IEEE Commun. Surv. Tut., vol. 18, no. 2, pp. 1123–1152, Apr.–Jun. 2016.

[49] C. M. Grinstead and J. L. Snell
Grinstead and Snell's Introduction to Probability. New Hampshire England, U.K.: Chance Project, 2006.

Haneya Naeem Qureshi (GS'16) received the B.S. degree in electrical engineering from the Lahore University of Management Sciences, Lahore, Pakistan, in 2016 and the M.S. degree in electrical and computer engineering in 2017 from The University of Oklahoma, Tulsa, OK, USA, where she is currently working toward the Ph.D. degree in electrical and computer engineering.

She is currently with the Artificial Intelligence for the Networks Laboratory, The University of Oklahoma, where she is contributing to several NSF funded projects. She has also been engaged in addressing channel estimation and pilot contamination problem in massive MIMO TDD systems. Her current research interests include network automation and combination of machine learning and analytics for future cellular systems.

Ali Imran (M'15–SM'17) received the B.Sc. degree in electrical engineering from the University of Engineering and Technology, Lahore, Pakistan, in 2005, and the M.Sc. degree (with distinction) in mobile and satellite communications and the Ph.D. degree in electrical and computer engineering from the University of Surrey, Guildford, U.K., in 2007 and 2011, respectively.

He is currently an Assistant Professor in telecommunications with The University of Oklahoma, Tulsa, OK, USA, where he is the Founding Director of the Artificial Intelligence for Networks Laboratory Research Center and TurboRAN 5G Testbed. He has been leading several multinational projects on self-organizing cellular networks, such as QSON, for which he has secured research grants of over 3 million in last four years as the Lead Principal Investigator. He is currently leading four NSF funded projects on 5G amounting to over 2.2 million. He has authored more than 60 peer-reviewed articles and presented a number of tutorials at international forums, such as the IEEE International Conference on Communications, the IEEE Wireless Communications and Networking Conference, the European Wireless Conference, and the International Conference on Cognitive Radio Oriented Wireless Networks, on his topics of interest. His research interests include self-organizing networks, radio resource management, and big-data analytics.

Dr. Imran is an Associate Fellow of the Higher Education Academy, U.K., and a member of the Advisory Board to the Special Technical Community on Big Data of the IEEE Computer Society.